



Calhoun: The NPS Institutional Archive
DSpace Repository

Faculty and Researchers

Faculty and Researchers' Publications

2021

Solutions of the Eliassen balance equation for inertially and/or symmetrically stable and unstable vortices

Wang, Shanghong; Montgomery, Michael T.; Smith, Roger K.

Royal Meteorological Society

Wang, Shanghong, Michael T. Montgomery, and Roger K. Smith. "Solutions of the Eliassen balance equation for inertially and/or symmetrically stable and unstable vortices." *Quarterly Journal of the Royal Meteorological Society* (2020).

<https://hdl.handle.net/10945/67449>

This publication is a work of the U.S. Government as defined in Title 17, United States Code, Section 101. Copyright protection is not available for this work in the United States.

Downloaded from NPS Archive: Calhoun






Calhoun is the Naval Postgraduate School's public access digital repository for research materials and institutional publications created by the NPS community. Calhoun is named for Professor of Mathematics Guy K. Calhoun, NPS's first appointed -- and published -- scholarly author.

Dudley Knox Library / Naval Postgraduate School
411 Dyer Road / 1 University Circle
Monterey, California USA 93943

<http://www.nps.edu/library>

RESEARCH ARTICLE

Solutions of the Eliassen balance equation for inertially and/or symmetrically stable and unstable vortices

Shanghong Wang^{1,2}  | Michael T. Montgomery³  | Roger K. Smith¹ 

¹Meteorological Institute,
Ludwig-Maximilians University of
Munich, Munich, Germany

²Shanghai Typhoon Institute, China
Meteorological Administration, Shanghai,
China

³Department of Meteorology, Naval
Postgraduate School, Monterey, California

Correspondence

M. T. Montgomery, Department of
Meteorology, Naval Postgraduate School,
Monterey, 93943 CA, USA.
Email: mtmontgo@nps.edu

Funding information

NSF ONR, Grant/Award Numbers:
AGS-1313948, IAA-1656075,
N0001420WX01473

Abstract

Two methods for solving the Eliassen equation for the corresponding balanced secondary circulation of a numerically simulated, high-resolution tropical cyclone vortex are compared. In idealized calculations for a symmetrically stable vortex, both methods (successive overrelaxation [SOR] and multigrid) converge and the solutions are broadly similar. In more typical cases, where the vortex has regions of inertial or symmetric instability, it is necessary to coarsen the data from the numerical simulation to determine the balanced secondary circulation. A convergent solution can be obtained with the multigrid method for a finer grid spacing than with the SOR method. However, the multigrid method fails to converge when the vertical grid spacing is similar to that of the numerical simulation. Results using both methods confirm the inability of the balance formulation to capture the strong inflow and resulting tangential wind spin-up in the frictional boundary layer during a period of rapid intensification. Typical tropical cyclone simulations show an inflow layer just beneath the upper-level outflow layer, and the corresponding balanced secondary circulation may show such an inflow layer also. However, caution is called for in attributing this inflow layer to a balanced flow response driven by the distribution of diabatic heating and tangential momentum forcing. Our study suggests that this inflow layer is likely an artifact of the ad hoc regularization procedure that is necessary to keep the Eliassen equation globally elliptic in regions of inertial and/or symmetric instability.

KEYWORDS

hurricane, tropical cyclone, typhoon

1 | INTRODUCTION

For a slowly evolving tropical cyclone vortex in which flow asymmetries are not a dominant factor, a well-known approximate description of the slow evolution is furnished by the Eliassen balance vortex model (Willoughby, 1979; Schubert and Hack 1982, Shapiro and Willoughby 1982, Smith *et al.*, 2018, and refs.). In this reduced model, the

tropical cyclone vortex is represented to leading order by the primary (tangential) circulation about the cyclone center. Superposed on the primary circulation is a secondary (overturning) circulation, which is typically inwards in the lower troposphere and outwards in the upper troposphere. The secondary circulation is driven primarily by the aggregate of latent heat release in deep cumulus convection in the central convection zone of the vortex.

Assuming that the tropical cyclone is in strict gradient and hydrostatic balance, the secondary circulation can be diagnosed by solving a partial differential equation in the radius–height plane for the meridional streamfunction (the so-called Eliassen equation for the transverse circulation). This equation governs the overturning circulation that is required to keep the vortex in a state of persistent thermal wind balance as the tangential momentum forcing and thermodynamic heat forcing tries to drive the vortex out of balance. Previous work has suggested that this balance model is sufficient to describe the secondary circulation in an intensifying tropical cyclone, including in the vortex boundary layer (Heng *et al.* 2017). However, this assertion has been rebutted by Montgomery and Smith (2018), who noted, *inter alia*, that Heng *et al.* did not solve a strictly balance vortex model and inadvertently ignored the derivational requirement that the basic state vortex remain in a state of strict thermal wind balance during the vortex evolution.

Heng *et al.* (2018) attempted to rebut the critique of Montgomery and Smith (2018) by solving the Eliassen equation for a single numerical simulation, but again employed basic state vortices that are not in strict thermal wind balance. Recent work by Montgomery and Persing (2020) has confirmed prior findings of Bui *et al.* (2009) and Abarca and Montgomery (2014) demonstrating that the strict Eliassen balance model fails to represent the strong inflow in the boundary layer needed to generate the intensifying tangential winds.

Most previous solutions of the Eliassen equation have been obtained using the SOR method, including those in the aforementioned papers. Recent work by Wang *et al.* (2020) using a particularly high spatial resolution simulation of an intensifying tropical cyclone has found that balance solutions can be obtained only by using a coarsened resolution representation of the simulated vortex. This work affirms and underscores the findings of Montgomery and Persing (2020) and raises a new question of whether axisymmetric balance dynamics is robustly meaningful in high-resolution simulations of tropical cyclone intensification. By robustly meaningful we mean that a solution actually exists. A particular problem is that, as shown by Smith *et al.* (2018), the evolution of a vortex in a balanced formulation develops regions of inertial instability in which the Eliassen equation becomes hyperbolic. In an attempt to overcome this problem, it is necessary to modify the coefficients of the Eliassen equation in these regions so that the equation remains globally elliptic. The procedure for carrying out this modification, often referred to as “regularization”, is necessarily *ad hoc*. Even if a mathematical solution of the regularized Eliassen equation could be shown to exist, an extensive region of regularization may be a reason

for the SOR method to fail, unless the resolution of the model data in the Eliassen equation are coarsened.

As a first step in verifying the robustness of their findings, Wang *et al.* (2020) used an independent multigrid solution method for solving the Eliassen equation. The purpose of this study is threefold: (a) to document the details of the computational methods used in Wang *et al.* (2020), (b) to explore the sensitivity of the solutions to the particular method used, and (c) to assess the robustness of conclusions based on the SOR method. A specific question addressed is whether a convergent solution of the Eliassen equation for a high-resolution simulation can be obtained using a multigrid method when the straightforward SOR method fails.

We describe the calculations performed in Section 2 and review briefly the SOR method and the more sophisticated multigrid method in Section 3. The results of various calculations are presented in Section 4. The conclusions are presented in Section 5.

2 | CALCULATIONS

In axisymmetric cylindrical coordinates (r, z) , the Eliassen equation for the streamfunction ψ of the secondary circulation has the following form (as in Montgomery and Persing 2020):

$$\frac{\partial}{\partial r} \left[\bar{A} \frac{\partial \psi}{\partial r} + \frac{1}{2} \bar{B} \frac{\partial \psi}{\partial z} \right] + \frac{\partial}{\partial z} \left[\bar{C} \frac{\partial \psi}{\partial z} + \frac{1}{2} \bar{B} \frac{\partial \psi}{\partial r} \right] = \dot{\Theta}, \quad (1)$$

where

$$\bar{A} = -g \frac{\partial \chi}{\partial z} \frac{1}{\rho r} = \left(\frac{\chi}{\rho r} \right) N^2, \quad (2)$$

$$\bar{B} = -\frac{2}{\rho r} \frac{\partial}{\partial z} (\chi C) = -\frac{2}{\rho r} \left(\chi \xi \frac{\partial v}{\partial z} + C \frac{\partial \chi}{\partial z} \right), \quad (3)$$

$$\bar{C} = \left(\xi (\zeta + f) \chi + C \frac{\partial \chi}{\partial r} \right) \frac{1}{\rho r} = \frac{\chi}{\rho r} I_g^2, \quad (4)$$

and

$$\dot{\Theta} = g \frac{\partial}{\partial r} (\chi^2 \dot{\theta}) + \frac{\partial}{\partial z} (C \chi^2 \dot{\theta}) + \frac{\partial}{\partial z} (\chi \xi \dot{V}), \quad (5)$$

where v is the tangential velocity component, $\chi = 1/\theta$ is the inverse of the potential temperature, $C = v^2/r + fv$ is the sum of centrifugal and Coriolis forces per unit mass, $\xi = f + 2v/r$ is twice the local absolute angular velocity, f is the Coriolis parameter (assumed constant), g is the acceleration due to gravity, $\zeta = (1/r)\partial(rv)/\partial r$ is the vertical component of relative vorticity, N^2 is the square of the Brunt–Väisälä frequency, defined as $(g/\theta)\partial\theta/\partial z$, and $I_g^2 = \xi(\zeta + f) + (C/\chi)\partial\chi/\partial r$ is the square of the generalized

inertial frequency. The quantities \bar{A} and \bar{C} are proportional to the static stability and inertial stability, respectively. Here it is understood that the coefficient variables of the Eliassen equation above are associated with the azimuthal wavenumber zero component of the flow in a three-dimensional numerical simulation about some nominal centre. The quantity \bar{B} characterizes, in part, the strength of the vertical shear of the gradient wind. The net forcing term $\hat{\Theta}$ as defined by Equation 5 represents a combination of the diabatic heating and momentum forcing, $\hat{\theta}$ and \hat{V} , respectively.

The discriminant of Equation 1, Δ , is given by

$$\Delta = 4\bar{A}\bar{C} - \bar{B}^2. \quad (6)$$

The equation is locally elliptic if $\Delta > 0$, locally hyperbolic if $\Delta < 0$, and locally parabolic if $\Delta = 0$.¹

In the anelastic approximation, the transverse velocity components u and w are given in terms of ψ by

$$u = -\frac{1}{r\rho} \frac{\partial \psi}{\partial z}, \quad w = \frac{1}{r\rho} \frac{\partial \psi}{\partial r}. \quad (7)$$

Four sets of calculations are carried out to compare the balance solutions for the streamfunction of the secondary circulation of tropical-cyclone-like flows obtained using the SOR and multigrid solution methods.

The first set of calculations, referred to as Calc-A, relate to the balanced streamfunction of an idealized tropical-cyclone-like vortex defined by a specified tangential wind profile, $v(r, z)$, forced by a specified distribution of diabatic heating rate $\hat{\theta}(r, z)$, where

$$v(r, z) = V_m \left(\frac{r}{r_m} \right) \exp \left[\frac{1}{b} \left(1 - \left(\frac{r}{r_m} \right)^b \right) \right] \cos \left(\frac{\pi z}{2z_d} \right), \quad (8)$$

with $b = 0.45$, $V_m = 60 \text{ m}\cdot\text{s}^{-1}$, $r_m = 30 \text{ km}$, $z_d = 18 \text{ km}$, and

$$\begin{aligned} \hat{\theta}(r, z) &= \hat{\theta}_0 \cos \left(\frac{1}{2} \pi \frac{\delta r}{r_c} \right) \cos \left(\frac{1}{2} \pi \frac{\delta z}{z_c} \right) \\ &\quad (|r - r_c| < r_w \text{ and } |z - z_c| < z_c) \\ &= 0 \quad \text{elsewhere,} \end{aligned} \quad (9)$$

with $\delta r = r - r_c$, $\delta z = z - z_c$, $r_c = 30 \text{ km}$, $z_c = 8 \text{ km}$, and $r_w = 20 \text{ km}$. In these formulae: V_m is the maximum tangential wind speed, which occurs at the surface at radius r_m ; r_c and z_c are the radius and height of the maximum diabatic heating; $\hat{\theta}_0 = 70 \text{ K}\cdot\text{hr}^{-1}$ is the maximum amplitude of the heating rate, r_w is the width of the heating function which

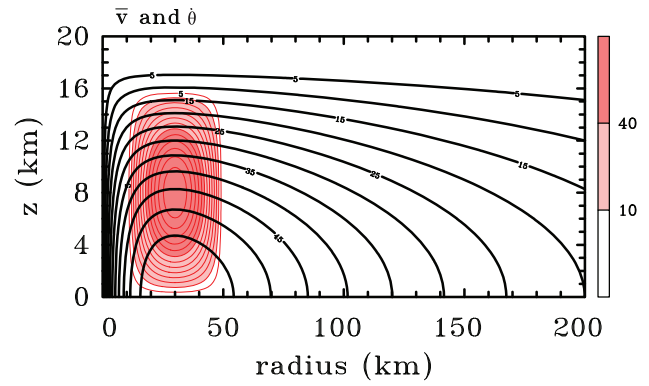


FIGURE 1 Tangential velocity v (thick black contour intervals of $5 \text{ m}\cdot\text{s}^{-1}$) of an idealized tropical-cyclone-like vortex with a prescribed diabatic heating, $\hat{\theta}(r, z)$ (shaded, contour interval $5 \text{ K}\cdot\text{hr}^{-1}$) [Colour figure can be viewed at wileyonlinelibrary.com]

is 20 km . The tangential wind decreases sinusoidally with height to an altitude of $z_d = 18 \text{ km}$ and is set to zero above 18 km . There is no momentum forcing in these particular calculations. The structure of tangential wind and diabatic heating is shown in Figure 1.

The second set of calculations, Calc-B, relate to the balanced secondary circulation at 60 hr of the simulation in Wang *et al.* (2020). In this simulation, the horizontal grid spacing is 1 km and there are 78 vertical levels from 0 to 25 km . The vertical grid spacing is 100 m in the first 1 km and 500 m from 16 to 25 km . Between 1 and 16 km , the grid is stretched uniformly. For the present calculations, the output data are interpolated to a new fine grid in a region 400 km square in the horizontal and 20 km in the vertical using bicubic splines. This new grid retains a horizontal grid spacing of 1 km , but the vertical grid spacing is 50 m . The tangential wind field is azimuthally averaged and time-averaged for 1 hr using 1 min output data. The corresponding balanced pressure and temperature distribution are obtained by using the unapproximated method of Smith (2006), assuming a latitude of 20°N and the Dunion moist tropical sounding (Dunion, 2011) at some large radius.

The third set of calculations, Calc-C, relate to the balanced secondary circulation of the vortex structure in Wang *et al.* (2020) at 60 hr , but with the prescribed diabatic heating rate in Calc-A, while the fourth set of calculations Calc-D relate to the balanced secondary circulation of the vortex structure in Calc-A, but with the diabatic heating and momentum forcing in Wang *et al.* (2020) at 60 hr . The full set of calculations is summarized in Table 1.

Each set of calculations is performed with the SOR and multigrid methods with different radial and/or vertical resolution. To meet the special requirements of the multigrid method in relation to the number of grid points,

¹In Wang and Smith (2019), the coefficient \bar{B} is half that defined here and the discriminant is $\bar{A}\bar{C} - \bar{B}^2$.

TABLE 1 Summary of all calculations

Calculation	Vortex	Forcing
Calc-A	Ideal	Ideal
Calc-B	Model	Model
Calc-C	Model	Ideal
Calc-D	Ideal	Model

TABLE 2 Number of nonelliptic points ($\Delta \leq 0$) in Calc-B (and Calc-C) for different radial and vertical grid spacings, dr and dz , respectively

Nonelliptic	$dz = 600 \text{ m}$	$dz = 300 \text{ m}$	$dz = 150 \text{ m}$
$dr = 2 \text{ km}$	558	1,273	2,517
$dr = 1 \text{ km}$	1,119	2,559	5,064

the computational domain of each case consists of a cylindrical region 256 km in radius and 19.2 km in height.

Table 2 presents the number of nonelliptic points in Calc-B and Calc-C. It is clear that the number of nonelliptic grid points increases with decreasing grid spacing. Figure 2 shows that the negative discriminant area is broader at the finest resolution (panel (b)) than at the coarsest resolution (panel (a)), especially in the upper troposphere. Furthermore, the regions of static and symmetric instability are somewhat more extensive in the upper troposphere. It is foreseeable that the increase in negative discriminant area in the case of higher resolution might lead to additional difficulty in solving the Eliassen equation. The regularization scheme for the regions with negative discriminant is as follows: if $\bar{A} < 0$, \bar{A} is set equal to $\bar{B}^2/3.99\bar{C}$. If $\bar{C} < 0$, \bar{C} is set equal to $\bar{B}^2/3.99\bar{A}$. At any points where the discriminant is still negative, \bar{B} is set equal to $\pm\sqrt{3.99\bar{A}\bar{C}}$, the sign being chosen to be the original sign of \bar{B} .

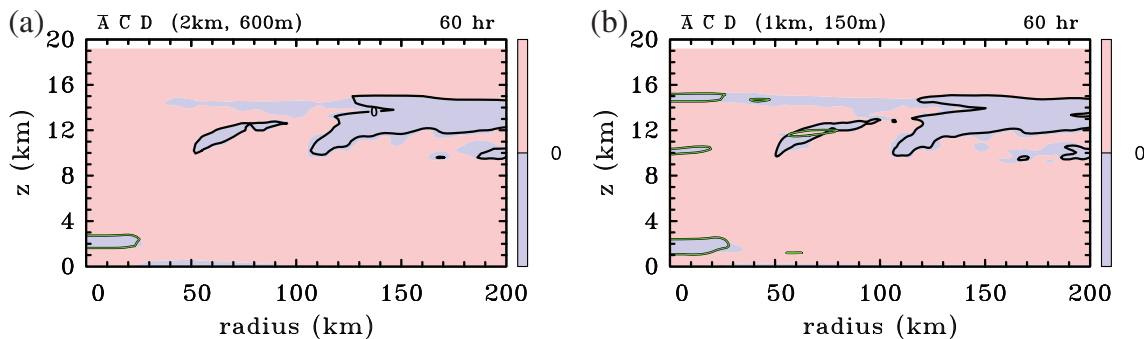


FIGURE 2 Sign of the coefficients \bar{A} , \bar{C} and the discriminant $\Delta = 4\bar{A}\bar{C} - \bar{B}^2$ in the Eliassen equation (1) for Calc-B (and Calc-C) with (a) $dr = 2 \text{ km}$, $dz = 600 \text{ m}$ and (b) $dr = 1 \text{ km}$, $dz = 150 \text{ m}$. The quantities \bar{A} and \bar{C} are proportional to the static stability and inertial stability, respectively, while the quantity \bar{B} characterizes, in part, the strength of the vertical shear of the gradient wind. \bar{A} (zero lines as green), \bar{C} (zero lines as black), and Δ (shaded, blue for negative, red for positive) [Colour figure can be viewed at wileyonlinelibrary.com]

3 | SOLUTION METHODS

3.1 | SOR method

On the discrete (r, z) mesh of points, the solver iterates for ψ by linearly marching through the grid mesh and minimizing the residual R defined by

$$R = \bar{A}\delta_{rr}\psi + \bar{B}\delta_{rz}\psi + \bar{C}\delta_{zz}\psi + \bar{D}\delta_r\psi + \bar{E}\delta_z\psi - \dot{\Theta}. \quad (10)$$

Here, the operator δ represents a discrete partial derivative in the direction of the subscript, with second-order derivatives having subscripts. The streamfunction at iteration step $k+1$ is obtained from that at step k by SOR:

$$\psi_{k+1} = \psi_k + \frac{\omega R_k}{2} \left[\frac{\bar{A}}{(\Delta r)^2} + \frac{\bar{C}}{(\Delta z)^2} \right]^{-1}, \quad (11)$$

where \bar{A} , \bar{B} , \bar{C} , and $\dot{\Theta}$ are defined in Section 2,

$$\bar{D} = \frac{\partial \bar{A}}{\partial r} + \frac{1}{2} \frac{\partial \bar{B}}{\partial z}, \quad (12)$$

$$\bar{E} = \frac{1}{2} \frac{\partial \bar{B}}{\partial r} + \frac{\partial \bar{C}}{\partial z}, \quad (13)$$

and $\omega = 1.8$ is the empirically chosen overrelaxation parameter (generally between 1.0 and 2.0). The iteration is deemed to have converged if the maximum difference in ψ between two iteration steps is less than 10^{-8} times the maximum magnitude of the solution at all interior (r, z) grid points. This criterion follows the suggestion of Adams 1991 in his multigrid method. Other technical details of the method can be found in Press *et al.* (1992) (pp. 866–870).

3.2 | Multigrid method

The multigrid (MG) method is an iteration method that has become quite popular and versatile for solving linear elliptic partial differential equations and even some nonlinear problems (Adams 1991). Although the method is not an overrelaxation method in the traditional sense, the method takes advantage of the fact that the residual error damps more quickly on small scales than larger scales of the grid mesh. The difference in error attenuation between the small and large scales allows one to cycle between small-scale and large-scale grids to accelerate the convergence rate of the solution. Specifically, the fine grid is used to eliminate the high-frequency oscillation error; the elimination of the low-frequency oscillation error is accomplished by the coarser grids, then the coarse-grid solution is projected back onto the fine grid, and this cycle is repeated until the residual decreases to a given error criterion. Because the convergence speed of the low-frequency oscillation error in the coarse grid is faster than on the original grid, the multigrid method is generally much faster than other classical, one-scale, iteration methods, such as SOR, Gauss–Siedel, or Jacobi iteration. The computational efficiency of the multigrid method is generally very high because the method scales in proportion to the number of grid points of the mesh. An excellent tutorial on multigrid methods and their relation to the classical one-scale iteration methods is provided by Briggs *et al.* (2000).

In the implementation of the multigrid method herein, the same convergence criterion is employed as for the SOR method discussed above.

4 | RESULTS

4.1 | Calculation set Calc-A

The set of 12 calculations Calc-A comprise six using the SOR method and six using the multigrid method with a combination of $dr=1$ km or 2 km and $dz=150, 300,$ or 600 m. Figure 3 shows the structure of the radial and vertical velocity components for a selection of these calculations. The 1 km radial grid spacing corresponds to the spacing in the model simulation used to generate the data for Calc-B. The panels in the left column show the solutions using the SOR method, while those in the right column show those using the multigrid method. From the figure, it is seen that the flow in all panels is essentially the same, confirming the integrity of both solution methods.

The maximum inflow occurs near the surface, while the maximum outflow occurs at a height of about 15 km. The strongest ascent occurs in the region of maximum

heating, a feature to be expected from the study of Shapiro and Willoughby (1982) and Smith *et al.* (2018). The maximum inflow for each of the 12 cases differs by no more than $0.2 \text{ m}\cdot\text{s}^{-1}$, while the maximum outflow differs by no more than $0.1 \text{ m}\cdot\text{s}^{-1}$. In essence, for this idealized case, the multigrid and SOR methods give essentially the same results, irrespective of grid spacing.

4.2 | Calculation set Calc-B

We turn now to examine in more depth the solutions for the balanced secondary circulation in the high-resolution tropical cyclone simulation presented by Wang *et al.* (2020) forced by the azimuthally averaged diabatic heating and tangential momentum forcing (including the eddy terms) diagnosed from the simulation at 60 hr. These forcing distributions are shown in figure 9b,c of Wang *et al.* (2020). Table 3 shows that, as the resolution increases, convergent solutions become harder to obtain. Figure 4 compares solutions for the balanced secondary circulation with different grid resolutions with the circulation obtained from the azimuthally averaged output from the simulation, itself, at 60 hr. Figure 4a shows the azimuthally averaged circulation in the simulation, while Figure 4b shows the corresponding balanced solution obtained using the SOR method with a radial grid spacing of 2 km and vertical grid spacing of 600 m. This choice of grid configuration is coarser than that used for the simulated vortex for reasons discussed in the “Introduction.”

As noted by Wang *et al.* (2020), the mean height of the balanced outflow is too low (12 km compared with 14 km) and the outflow is split at larger radii in the balance solution. There are strong discrepancies also in the strength and radial extent of the inflow layers. For example, the inflow below the upper outflow layer is approximately twice as strong in the balance solution and the inflow layer above the outflow layer is barely evident. The maximum radial velocity in the upper-level outflow in the balance solution is $23.3 \text{ m}\cdot\text{s}^{-1}$, compared with $20.3 \text{ m}\cdot\text{s}^{-1}$ in the simulation. The boundary layer inflow in the balance solution is significantly weaker than in the simulation (maximum inflow $7.5 \text{ m}\cdot\text{s}^{-1}$ compared with $24.5 \text{ m}\cdot\text{s}^{-1}$, a factor of three discrepancy), but is much deeper in the inner region as found by Montgomery and Persing (2020).

Figure 4c shows the balance solution using the multigrid method with the same grid configuration as in Figure 4b. Comparing Figure 4b,c it is seen that the multigrid solution is almost the same as that obtained with SOR. Indeed, the maximum upper-level outflow and inflow have comparable values (Table 4), but the outflow and inflow weaken slightly faster with radius with the multigrid method. Again, the boundary layer inflow in the

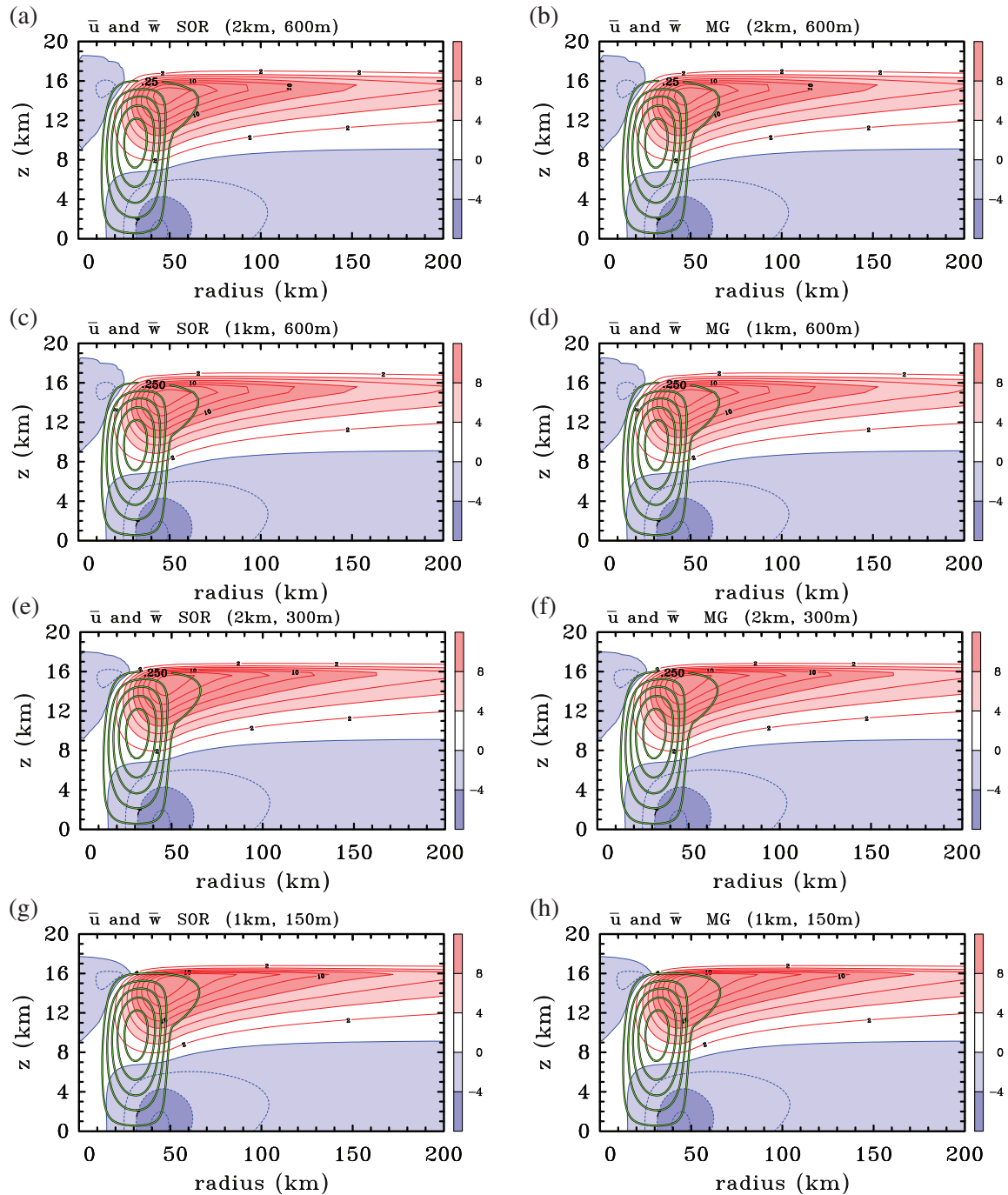


FIGURE 3 Axisymmetric balanced solutions for the radial (\bar{u}) and vertical (\bar{w}) components of the secondary circulation in a subset of Calc-A. The calculations differ in the method of solution (SOR in the left columns, MG in the right columns) and the radial and vertical grid spacing (dr, dz): (a, b) $dr = 2$ km, $dz = 600$ m; (c, d) $dr = 1$ km, $dz = 600$ m; (e, f) $dr = 2$ km, $dz = 300$ m; (g, h) $dr = 1$ km, $dz = 150$ m. Contour interval for \bar{u} : 2 m \cdot s $^{-1}$ when $\bar{u} > 0$, 1 m \cdot s $^{-1}$ when $\bar{u} < 0$. Positive contours solid, negative contours dashed. Shading values indicated on color bar. Green thick contours are shown for \bar{w} : 0.25 m \cdot s $^{-1}$ (only positive values are shown) [Colour figure can be viewed at wileyonlinelibrary.com]

balance solution is much weaker than in the numerical simulation, reflecting the fact that the balance assumption in the boundary layer is poor.

When the vertical grid spacing is halved, the SOR method failed to converge, but a convergent solution is still possible using the multigrid method (Figure 4d). However,

this solution is noticeably different in detail from that with the coarser vertical resolution in Figure 4c. The upper outflow layer has a stronger maximum and a more obvious two-layer structure at large radii. The upper inflow is stronger also and extends to a larger radius, even exceeding the strength of that in the numerical simulation.

TABLE 3 Summary of SOR and multigrid performance for Calc-B

Calc-B	SOR	MG
$dr = 2 \text{ km}, dz = 600 \text{ m}$	Solvable	Solvable
$dr = 2 \text{ km}, dz = 300 \text{ m}$	Unsolvable	Solvable
$dr = 2 \text{ km}, dz = 150 \text{ m}$	Unsolvable	Unsolvable
$dr = 1 \text{ km}, dz = 600 \text{ m}$	Unsolvable	Solvable
$dr = 1 \text{ km}, dz = 300 \text{ m}$	Unsolvable	Unsolvable
$dr = 1 \text{ km}, dz = 150 \text{ m}$	Unsolvable	Unsolvable

Although the maximum boundary layer inflow is larger also, its strength is still greatly underestimated relative to that of the simulation. When the vertical grid spacing is

halved again to 150 m, neither solution method converges (Table 3).

When the radial grid spacing is reduced to 1 km, the same as in the numerical simulation (Figure 4e), a convergent solution is possible only using the multigrid method and only then using the coarsest vertical grid spacing of 600 m. The solution in this case is virtually indistinguishable from that in Figure 4c.

Table 5 shows the root mean square error between the radial velocity in the model simulation and that in two of the balance solutions in Calc-B. The root mean square error (RMSE) is defined as

$$RMSE = \sqrt{\frac{1}{n} \sum_{i=1}^n (e_i)^2}, \quad (14)$$

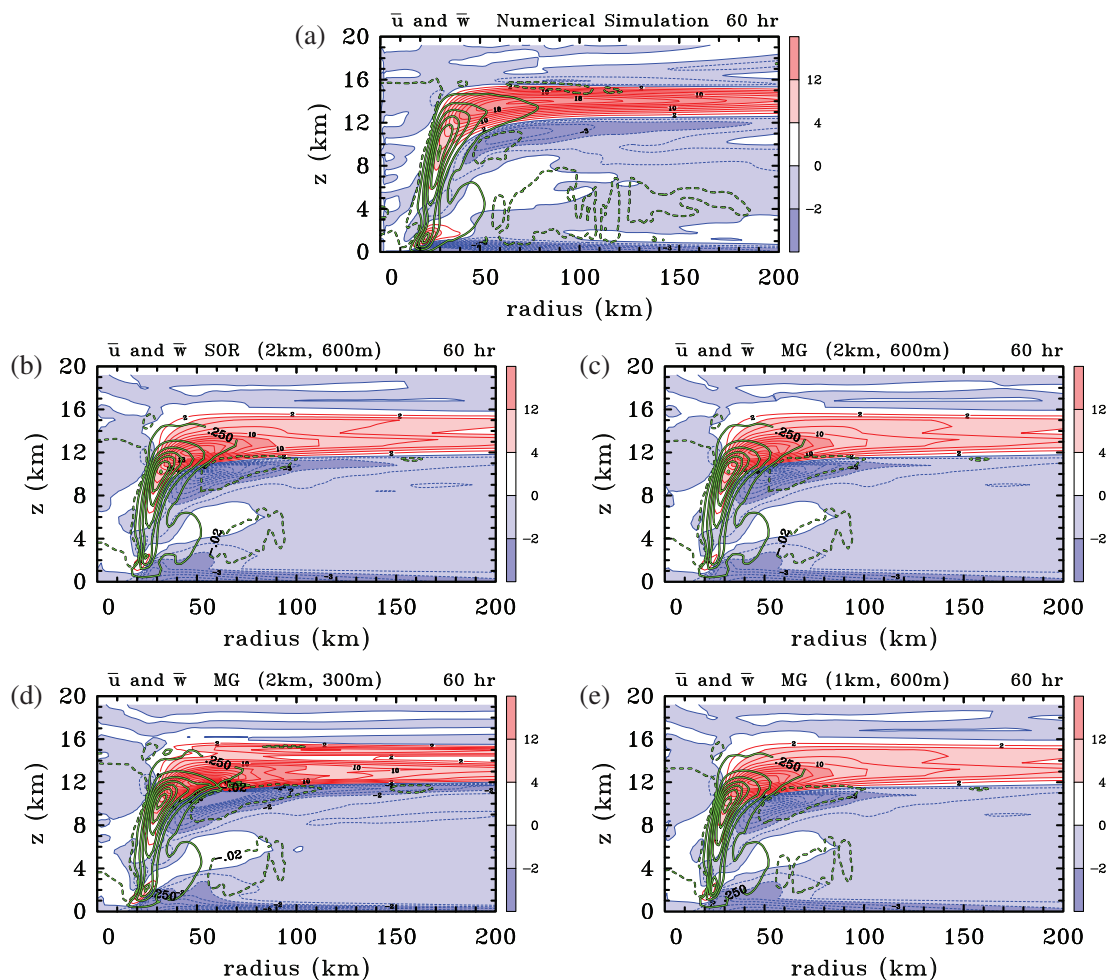


FIGURE 4 Axisymmetric balanced solutions for the radial (\bar{u}) and vertical (\bar{w}) components of the secondary circulation at 60 hr in the numerical simulation (a) and in a subset of axisymmetric balanced solutions for Calc-B. The fields in panels (a) are azimuthally averaged and time-averaged for 1 hr using 1 min output. (b) SOR and (c) MG with $dr = 2 \text{ km}, dz = 600 \text{ m}$; (e) MG with $dr = 2 \text{ km}, dz = 300 \text{ m}$; (f) MG with $dr = 1 \text{ km}, dz = 600 \text{ m}$. Contour interval for $2 \text{ m}\cdot\text{s}^{-1}$ when $\bar{u} > 0$, $1 \text{ m}\cdot\text{s}^{-1}$ when $\bar{u} < 0$. Positive contours solid, negative contours dashed. Shading values indicated on color bar. Only two thick contours are shown for \bar{w} . For $\bar{w} > 0$, $0.25 \text{ m}\cdot\text{s}^{-1}$ (green, solid); for $\bar{w} < 0$, $-0.02 \text{ m}\cdot\text{s}^{-1}$ (green, dashed). Shading values indicated on color bar [Colour figure can be viewed at wileyonlinelibrary.com]

TABLE 4 Maximum values of inflow and outflow for each case in Calc-B

Calc-B	Upper-max	Upper-min	Lower-min
Simulation	20.3 m·s ⁻¹	-4.9 m·s ⁻¹	-24.5 m·s ⁻¹
SOR, 2 km, 600 m	23.3 m·s ⁻¹	-10.2 m·s ⁻¹	-7.5 m·s ⁻¹
MG, 2 km, 600 m	22.8 m·s ⁻¹	-9.7 m·s ⁻¹	-7.5 m·s ⁻¹
MG, 2 km, 300 m	38.9 m·s ⁻¹	-14.8 m·s ⁻¹	-9.2 m·s ⁻¹
MG, 1 km, 600 m	22.8 m·s ⁻¹	-9.7 m·s ⁻¹	-7.5 m·s ⁻¹

TABLE 5 Point-by-point root mean square error between the radial velocity in the numerical simulation at 60 hr and that in two balance calculations of set Calc-B, those shown in Figure 4b,c

Calc-B/600 m-2 km	SOR	MG
Whole domain	3.1 m·s ⁻¹	3.0 m·s ⁻¹
Inside regularization region	6.3 m·s ⁻¹	6.0 m·s ⁻¹
Outside regularization region	2.1 m·s ⁻¹	2.1 m·s ⁻¹

where n is the number of sample points and e_i is the difference between the model simulation and balance solution. The two balance solutions are those obtained using the SOR method and multigrid method with a radial grid spacing of 2 km and a vertical grid spacing of 600 m shown in Figure 4b,c. In each calculation there are 3,333 grid points, 470 inside the regularization region ($\Delta < 0$) and 2,863 outside. For the SOR calculation, the RMSE is 3.1 m·s⁻¹ over the whole domain, 6.3 m·s⁻¹ inside the regularization region, and 2.1 m·s⁻¹ outside the regularization region. These error measures suggest that the agreement between the balance calculation and the simulation is rather poor. The RMSEs for the multigrid calculation are only marginally better than those for the SOR calculation, showing again that the balance calculation is rather poor for diagnosing the secondary circulation of the numerical simulation, especially in the region of regularization. These findings are in line with those in the studies by Wang and Smith (2019), Wang *et al.* (2020), and Montgomery and Persing (2020).

4.3 | Calculation set Calc-C

In an effort to pinpoint the reasons for the failure of the SOR and multigrid methods to converge for smaller grid spacings in calculation set Calc-B, we turn first to a set of calculations with the same vortex structure in Calc-B, but with the idealized forcing used in Calc-A. The tangential wind structure and prescribed diabatic heating rate used in Calc-C are shown in Figure 5a. As in Calc-B, there are regions where the discriminant of the Eliassen equation

is negative (Figure 2) and the equation requires regularization. Even though the diabatic heating rate in these calculations has a regular shape, the secondary circulation has more structure than in Figure 3 with an inflow layer beneath the upper-level outflow.

The two solutions with the same grid spacing are similar, with two local maxima in the upper-level outflow (Figure 5b,c). However, the multigrid solution with the same radial grid spacing, but with a vertical grid spacing of 300 m, has three local maxima within the outflow layer and a much stronger upper-level inflow (Figure 5d). As in Calc-B and as detailed in Table 6, the SOR method does not converge with a 300 m vertical grid spacing and neither solution method converges with a 150 m vertical grid spacing.

When the radial grid spacing is reduced to 1 km, it is only possible to obtain a solution with the multigrid method and only then with a vertical grid spacing of 600 m. This solution, which is shown in Figure 5e, is virtually the same as the solution with a 2 km radial grid spacing in Figure 5b. This result suggests that the solution is less sensitive to changes in the radial resolution than to changes in the vertical resolution, at least where a convergent solution is possible.

4.4 | Calculation set Calc-D

The final set of calculations, Calc-D, uses the full diabatic heating and momentum forcing (including that from the eddies) from the numerical simulation in Calc-B, (shown in figure 9b,c of Wang *et al.*, 2020), but incorporates the idealized vortex structure in Calc-A. The unique feature is that this vortex is everywhere symmetrically stable and the Eliassen equation does not require regularization. The balanced secondary circulation for this set of calculations is shown in Figure 6. The four calculations with 600 m vertical grid spacing and either 1 or 2 km radial grid spacing show similar structures with a hint of a second outflow maximum above the main outflow layer. The second outflow maximum is presumably related to the fine structure of the diabatic heating rate. With a vertical grid spacing of 300 m, the second outflow feature becomes more marked using both solution methods (panels (e) and (f)), while in the finest resolution solutions (panels (g) and (h)), the second outflow structure is even more pronounced.

Notably, there is no concentrated inflow layer below the main outflow layer as in Calc-B and Calc-C. This result indicates that the upper-level inflow layer in Calc-B and Calc-C is mainly a consequence of the need to regularize the coefficients of the Eliassen equation in regions of symmetric instability. The implications of this finding are discussed in the next section.

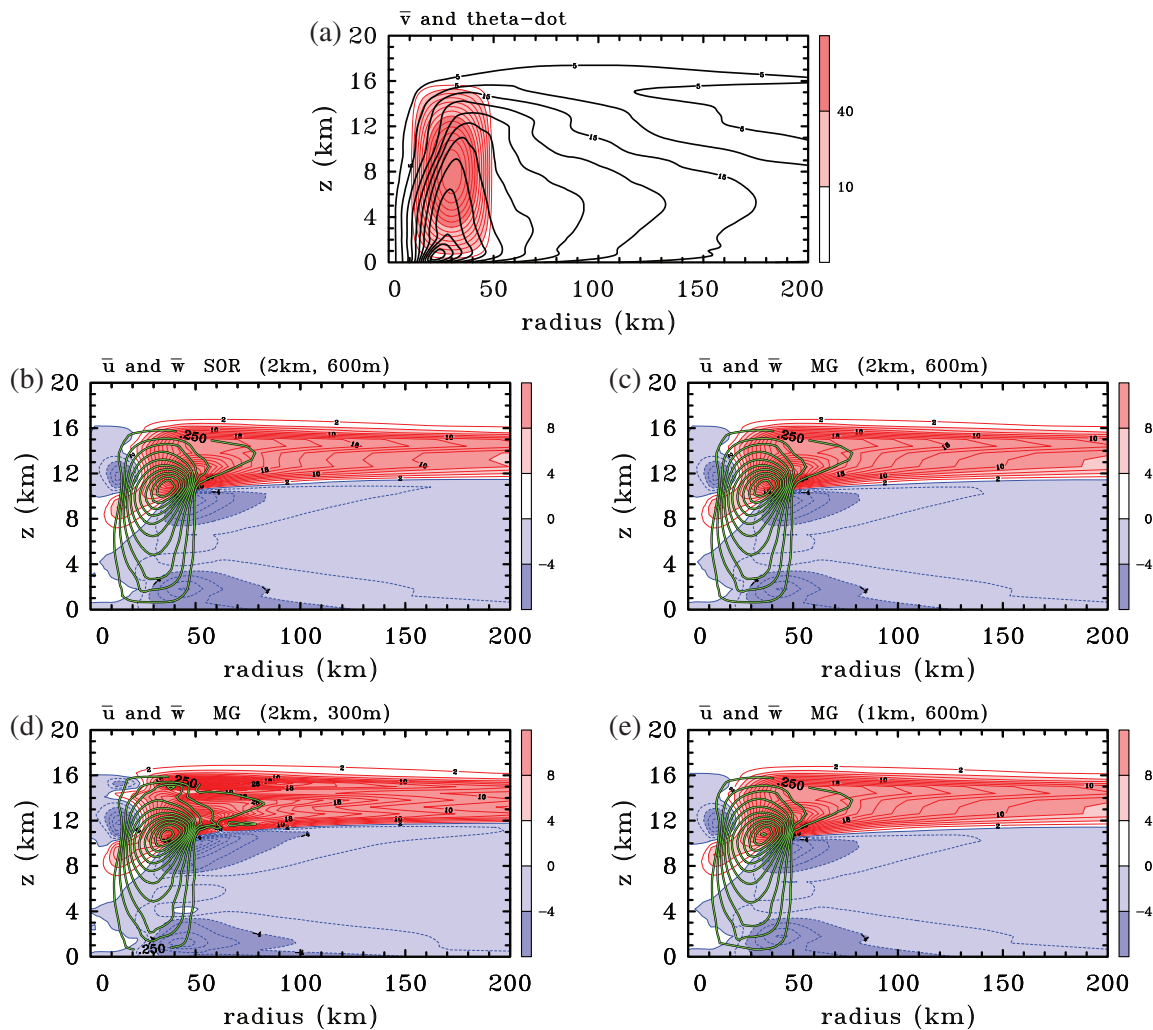


FIGURE 5 Axisymmetric balanced solutions for the radial (\bar{u}) and vertical (\bar{w}) components of the secondary circulation in a subset of Calc-C. For comparison, panel (a) shows the tangential wind from the numerical simulation at 60 hr and a prescribed diabatic heating rate ($\text{K}\cdot\text{hr}^{-1}$). (b) SOR method, $dr = 2 \text{ km}$, $dz = 600 \text{ m}$. Panels (c)–(e) use the MG method with (c) $dr = 2 \text{ km}$, $dz = 600 \text{ m}$; (d) $dr = 2 \text{ km}$, $dz = 300 \text{ m}$; (e) $dr = 1 \text{ km}$, $dz = 600 \text{ m}$. Contour interval for \bar{u} : $2 \text{ m}\cdot\text{s}^{-1}$ when $\bar{u} > 0$, $1 \text{ m}\cdot\text{s}^{-1}$ when $\bar{u} < 0$. Positive contours solid, negative contours dashed. Shading values indicated on color bar. Green thick contours are shown for \bar{w} : $0.25 \text{ m}\cdot\text{s}^{-1}$ (only positive values are shown) [Colour figure can be viewed at wileyonlinelibrary.com]

As shown in Table 7, when the resolution increases, flow extrema increase marginally. For the same resolution, both solution methods give essentially the same results. Most importantly, without the need to regularize the Eliassen equation, a convergent solution can be obtained using both solution methods.

4.5 | Summary of calculations

Taken together, the four sets of calculations described above indicate that the ability to obtain a convergent solution of the Eliassen equation for the balanced secondary circulation of a high-resolution simulated tropical cyclone is severely compromised by the presence of regions where the azimuthal flow is inertially and/or symmetrically

TABLE 6 Summary of SOR and multigrid performance for Calc-C

Calc-C	SOR	MG
$dr=2 \text{ km}$, $dz=600 \text{ m}$	Solvable	Solvable
$dr=2 \text{ km}$, $dz=300 \text{ m}$	Unsolvable	Solvable
$dr=2 \text{ km}$, $dz=150 \text{ m}$	Unsolvable	Unsolvable
$dr=1 \text{ km}$, $dz=600 \text{ m}$	Unsolvable	Solvable
$dr=1 \text{ km}$, $dz=300 \text{ m}$	Unsolvable	Unsolvable
$dr=1 \text{ km}$, $dz=150 \text{ m}$	Unsolvable	Unsolvable

unstable. Such regions are predominantly found in the upper troposphere (see, e.g., Smith *et al.*, 2018). By severely compromised, we mean that it is no longer possible to

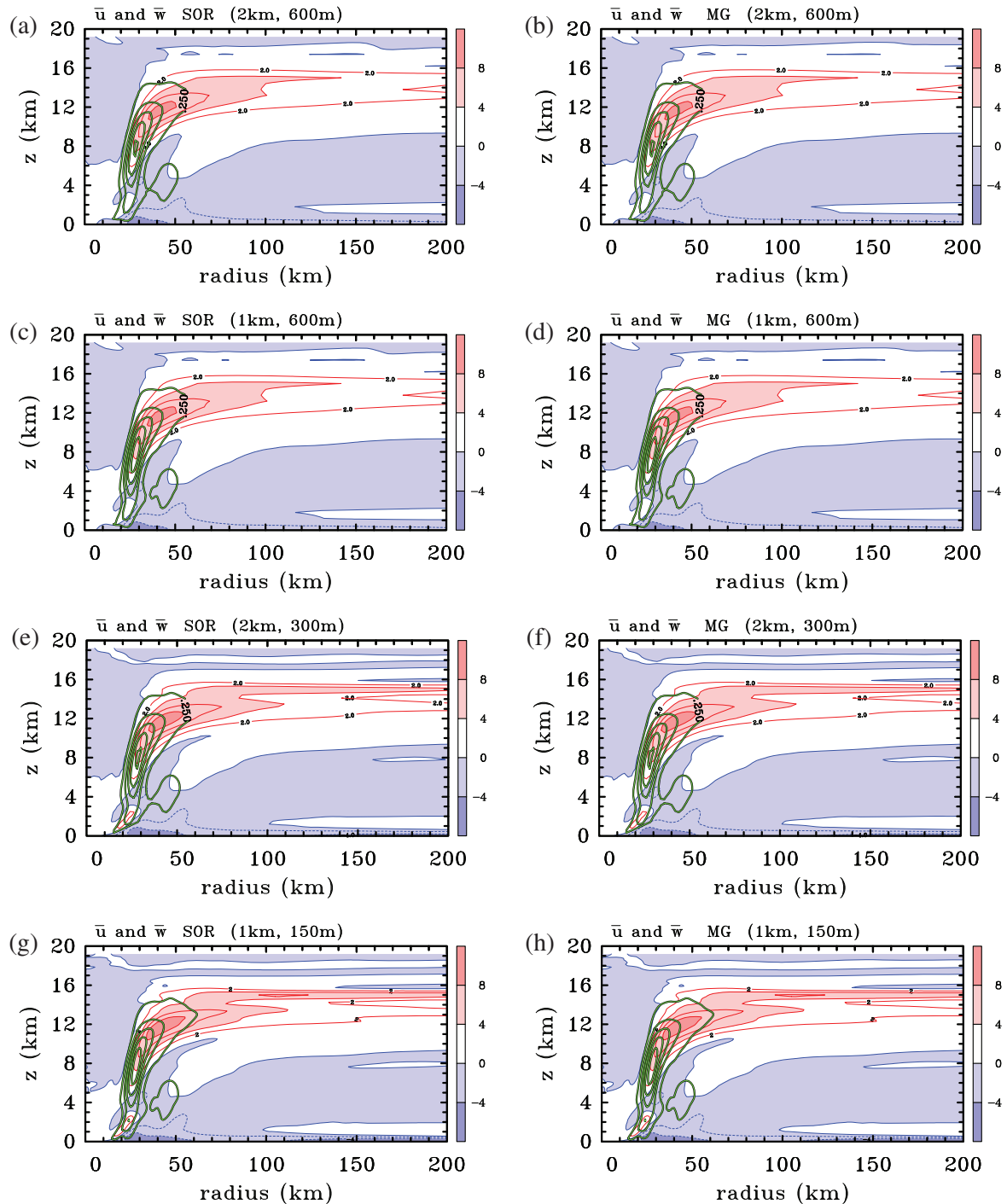


FIGURE 6 Axisymmetric balanced solutions for the radial (\bar{u}) and vertical (\bar{w}) components of the secondary circulation in a subset of Calc-D (idealized stable vortex, generalized diabatic heating [$\text{K} \cdot \text{hr}^{-1}$], and generalized tangential momentum forcing [$\text{m} \cdot \text{s}^{-1} \cdot \text{hr}^{-1}$]). The calculations differ in the method of solution (SOR in the left columns, MG in the right columns) and the radial and vertical grid spacing (dr, dz): (a, b) $dr = 2 \text{ km}$, $dz = 600 \text{ m}$; (c, d) $dr = 1 \text{ km}$, $dz = 600 \text{ m}$; (e, f) $dr = 2 \text{ km}$, $dz = 300 \text{ m}$; (g, h) $dr = 1 \text{ km}$, $dz = 150 \text{ m}$. Contour interval for \bar{u} : $2 \text{ m} \cdot \text{s}^{-1}$ when $\bar{u} > 0$, $1 \text{ m} \cdot \text{s}^{-1}$ when $\bar{u} < 0$. Positive contours solid, negative contours dashed. Shading values indicated on color bar. Green thick contours are shown for \bar{w} : $0.25 \text{ m} \cdot \text{s}^{-1}$ (only positive values are shown) [Colour figure can be viewed at wileyonlinelibrary.com]

obtain a convergent solution at a resolution commensurate with that of the simulation. In these situations, it is possible to obtain a convergent solution only by coarsening the grid, which serves to shrink the region of instability. With

this coarsening, the solutions obtained by the SOR and multigrid methods are essentially the same, but in the calculations carried out here, the multigrid method is capable of obtaining a convergent solution with a smaller radial

TABLE 7 Maximum values of upper-level inflow and outflow for each case in Calc-D

Calc-D	Outflow	Inflow
MG, $dr = 2$ km, $dz = 600$ m	$8.8 \text{ m}\cdot\text{s}^{-1}$	$-5.1 \text{ m}\cdot\text{s}^{-1}$
MG, $dr = 1$ km, $dz = 600$ m	$8.9 \text{ m}\cdot\text{s}^{-1}$	$-5.2 \text{ m}\cdot\text{s}^{-1}$
MG, $dr = 2$ km, $dz = 300$ m	$9.3 \text{ m}\cdot\text{s}^{-1}$	$-5.5 \text{ m}\cdot\text{s}^{-1}$
MG, $dr = 1$ km, $dz = 300$ m	$9.3 \text{ m}\cdot\text{s}^{-1}$	$-5.5 \text{ m}\cdot\text{s}^{-1}$
MG, $dr = 2$ km, $dz = 150$ m	$9.4 \text{ m}\cdot\text{s}^{-1}$	$-5.8 \text{ m}\cdot\text{s}^{-1}$
MG, $dr = 1$ km, $dz = 150$ m	$9.5 \text{ m}\cdot\text{s}^{-1}$	$-5.9 \text{ m}\cdot\text{s}^{-1}$
SOR, $dr = 2$ km, $dz = 600$ m	$8.8 \text{ m}\cdot\text{s}^{-1}$	$-5.1 \text{ m}\cdot\text{s}^{-1}$
SOR, $dr = 1$ km, $dz = 600$ m	$8.9 \text{ m}\cdot\text{s}^{-1}$	$-5.2 \text{ m}\cdot\text{s}^{-1}$
SOR, $dr = 2$ km, $dz = 300$ m	$9.3 \text{ m}\cdot\text{s}^{-1}$	$-5.5 \text{ m}\cdot\text{s}^{-1}$
SOR, $dr = 1$ km, $dz = 300$ m	$9.4 \text{ m}\cdot\text{s}^{-1}$	$-5.6 \text{ m}\cdot\text{s}^{-1}$
SOR, $dr = 2$ km, $dz = 150$ m	$9.4 \text{ m}\cdot\text{s}^{-1}$	$-5.8 \text{ m}\cdot\text{s}^{-1}$
SOR, $dr = 1$ km, $dz = 150$ m	$9.5 \text{ m}\cdot\text{s}^{-1}$	$-5.9 \text{ m}\cdot\text{s}^{-1}$

and/or vertical grid spacing than the SOR method, before it too fails to converge.

Comparison between the two sets of calculations Calc-C and Calc-D suggest that the inflow layer just beneath the upper-level outflow layer in the balance solution Calc-C is a consequence of the regularization that is required in this calculation, but not in Calc-D. Because regularization is an ad hoc procedure, this result calls for caution in attributing such inflow layers to a balanced flow response driven by the distribution of diabatic heating and tangential momentum forcing. It follows that an explanation of the upper-level inflow layers that are found in numerical simulations of tropical cyclones needs to be based on more fundamental considerations than assuming global thermal wind balance (Wang *et al.*, 2020).

The subset of calculations Calc-B that converge affirm prior work of Bui *et al.* (2009), Abarca and Montgomery (2014), Montgomery and Persing (2020), Wang and Smith (2019) and Wang *et al.* (2020) in that the boundary layer inflow in the strict axisymmetric Eliassen balance model is far too weak (by a factor of about 3) compared with the simulated inflow in the inner-core region of the vortex. It follows that the Eliassen balance model is unable to represent the nonlinear boundary layer spin-up mechanism that is essential for properly capturing the intensification of the maximum tangential wind of a tropical cyclone when realistic subgrid-scale diffusivities are employed. These results are further evidence to refute the claim by Heng *et al.* (2017; 2018) that the balance dynamics is sufficient to capture the secondary circulation

of an intensifying tropical cyclone, including the boundary layer.

5 | CONCLUSIONS

We have compared two solution methods, the SOR method and a multigrid method, to solve the Eliassen equation for the balanced secondary circulation of a tropical cyclone vortex for a particular forcing distribution of diabatic heating and tangential momentum forcing. These solutions confirm prior findings concerning the need to coarsen the data from high-resolution numerical simulations in the presence of inertial or symmetric instability when determining the corresponding balanced secondary circulation. They show also that the multigrid method is able to obtain a convergent solution with a finer grid spacing than the SOR method, although it too fails when the grid spacing is too small. When the vortex is symmetrically stable and both methods converge, the solutions are essentially the same.

The calculations suggest that the strong inflow layer just beneath the upper-level outflow layer in a balance flow solution of the Eliassen equation corresponding to a typical tropical cyclone simulation is a consequence of the need to regularize this equation in regions of inertial and/or symmetric instability. Because regularization is an ad hoc procedure, this inference calls for caution in attributing such inflow layers to a balanced flow response driven by the distribution of diabatic heating and tangential momentum forcing. Thus, an explanation of the upper-level inflow layers that are found in numerical simulations of tropical cyclones needs to be based on more fundamental considerations than assuming global thermal wind balance.

ACKNOWLEDGMENTS

M.T.M. acknowledges the support of NSF grants AGS-1313948, IAA-1656075, ONR grants N0001417WX00336 and N0001420WX01473 and the U.S. Naval Postgraduate School. The views expressed herein are those of the authors and do not represent sponsoring agencies or institutions. S.W. acknowledges a PhD stipend from the China Scholarship Council.

ORCID

Shanghong Wang  <https://orcid.org/0000-0002-0773-3448>

Michael T. Montgomery  <https://orcid.org/0000-0001-5383-4648>

Roger K. Smith  <https://orcid.org/0000-0002-3668-1608>

REFERENCES

- Abarca, S.F. and Montgomery, M.T. (2014) Departures from axisymmetric balance dynamics during secondary eyewall formation. *Journal of the Atmospheric Sciences*, 71, 3723–3738.
- Adams, J.C. (1991) *MUltigriD Software for Elliptic Partial Differential Equations: MUDPACK No. 357*. National Center for Atmospheric Research.
- Briggs, W.L., Hensen, V.E. and McCormick, S.F. (2000) *A Multigrid Tutorial* (2nd edition), (p. 193). Society for Industrial and Applied Mathematics.
- Bui, H.H., Smith, R.K., Montgomery, M.T. and Peng, J. (2009) Balanced and unbalanced aspects of tropical-cyclone intensification. *Quarterly Journal of the Royal Meteorological Society*, 135, 1715–1731.
- Dunion, J.P. (2011) Rewriting the climatology of the tropical North Atlantic and Caribbean Sea atmosphere. *Journal of Climate*, 24, 893–908.
- Heng, J., Wang, Y. and Zhou, W. (2017) Revisiting the balanced and unbalanced aspects of tropical cyclone intensification. *Journal of the Atmospheric Sciences*, 74, 2575–2591.
- Heng, J., Wang, Y. and Zhou, W. (2018) Reply to “comments on ‘revisiting the balanced and unbalanced aspects of tropical cyclone intensification’”. *Journal of the Atmospheric Sciences*, 75, 2497–2505.
- Montgomery, M.T. and Persing, J. (2020) Does balance dynamics well capture the secondary circulation and spin-up of a simulated tropical cyclone?. *Journal of the Atmospheric Sciences*, 78, 75–95.
- Montgomery, M.T. and Smith, R.K. (2018) Comments on: “Revisiting the balanced and unbalanced aspects of tropical cyclone intensification”. *Journal of the Atmospheric Sciences*, 75, 2491–2496.
- Press, W.H., S. A. Teukolsky, W. T. Vetterling and B. P. Flannery (1992) *Numerical Recipes in C: The Art of Scientific Computing*, (p. 994). Cambridge, UK: Cambridge University Press. ISBN-13:978-1107404083.
- Schubert, W.H. and Hack, J.J. (1982) Inertial stability and tropical cyclone development. *Journal of the Atmospheric Sciences*, 39, 1687–1697.
- Shapiro, L.J. and Willoughby, H.E. (1982) The response of balanced hurricanes to local sources of heat and momentum. *Journal of the Atmospheric Sciences*, 39, 378–394.
- Smith, R.K. (2006) Accurate determination of a balanced axisymmetric vortex. *Tellus A*, 58, 98–103.
- Smith, R.K., Montgomery, M.T. and Bui, H. (2018) Axisymmetric balance dynamics of tropical cyclone intensification and its breakdown revisited. *Journal of the Atmospheric Sciences*, 75, 3169–3189.
- Wang, S. and Smith, R.K. (2019) Consequences of regularizing the Sawyer-Eliassen equation in balance models for tropical cyclone behaviour. *Quarterly Journal of the Royal Meteorological Society*, 145, 3766–3779.
- Wang, S., Smith, R.K. and Montgomery, M.T. (2020) Upper-tropospheric inflow layers in tropical cyclones. *Quarterly Journal of the Royal Meteorological Society*, 146, 3466–3487.
- Willoughby, H.E. (1979) Forced secondary circulations in hurricanes. *Journal of Geophysical Research*, 84, 3173–3183.

How to cite this article: Wang, S., Montgomery, M.T. & Smith, R.K. (2021) Solutions of the Eliassen balance equation for inertially and/or symmetrically stable and unstable vortices. *Quarterly Journal of the Royal Meteorological Society*, 1–12. Available from: <https://doi.org/10.1002/qj.4098>